Author(s): Lindgren, Johan; Hulkko, Eero; Pettersson, Mika; Kiljunen, Toni

Title: Rotational coherence imaging and control for CN molecules through time-frequency resolved coherent anti-Stokes Raman scattering

Year: 2011

Version:

Please cite the original version:

Lindgren, J., Hulkko, E., Pettersson, M., & Kiljunen, T. (2011). Rotational coherence imaging and control for CN molecules through time-frequency resolved coherent anti-Stokes Raman scattering. The Journal of Chemical Physics, 135(22), 224514-8. https://doi.org/10.1063/1.3665934

Rotational coherence imaging and control for CN molecules through time-frequency resolved coherent anti-Stokes Raman scattering

Johan Lindgren, Eero Hulkko, Mika Pettersson, and Toni Kiljunen[a)]
Department of Chemistry, Nanoscience Center, P.O. Box 35, FI-40014 University of Jyväskylä, Finland

(Received 27 September 2011; accepted 15 November 2011; published online 13 December 2011)

Numerical wave packet simulations are performed for studying coherent anti-Stokes Raman scattering (CARS) for CN radicals. Electronic coherence is created by femtosecond laser pulses between the $X^2\Sigma$ and $B^2\Sigma$ states. Due to the large energy separation of vibrational states, the wave packets are superpositions of rotational states only. This allows for a specially detailed inspection of the second- and third-order coherences by a two-dimensional imaging approach. We present the time-frequency domain images to illustrate the intra- and intermolecular interferences, and discuss the procedure to rationally control and experimentally detect the interferograms in solid Xe environment. © *2011 American Institute of Physics*. [doi:10.1063/1.3665934]

I. INTRODUCTION

Quantum coherence and control are central aspects in coherent anti-Stokes Raman scattering (CARS), a special spectroscopic tool in a family of four-wave mixing (FWM) methods that utilize the operation of timed laser pulse sequences. Dynamics of electronic, vibrational, and rotational wave packets are the material responses to the engineered ultrashort laser pulses, amenable to control by the selection of wavelengths and pulse shapes. Optical control of molecular processes can be considered to lie at the core of the modern laser spectroscopy, see Ref. 1 for a perspective.

In condensed phases, where many important processes take place, a coherence based control tool is posed with challenges due to many-body interactions with surroundings.[2] Bimolecular reaction control, for example, is yet to be demonstrated in solid state conditions.[3,4] A simpler task is to affect mere physical properties within an ensemble of molecules by forming a wave packet of definitive phase information and content, and to probe the result during the coherence lifetime. Compared to studies on vibrational coherence,[5] focusing on the rotational states of molecular impurities is a much more rarely witnessed point of view. In the gas phase, however, rotational coherence spectroscopy is a mature research field,[6] and controlling molecular bond alignment and orientation is experiencing a rapid progression.[3,7]

Here we enter the wave packet interferometry aspect of rotations interrogated by the transient grating method in fs time scale. The interference-based detection of electronic polarizations and excited state populations has recently been reviewed by Cina,[8] Ohmori,[9] and Katsuki *et al.*,[10] where rotation-specific work can be found to be performed at least for Li_2 and I_2 molecules.[11,12] A new concept termed strong-laser-induced interference was introduced by Goto *et al.*[13] to incorporate multiple eigenstates into the time propagation of a single eigenstate. The mechanism is general and should be applicable for rotational eigenstates as well. It shows promise both for coherent control purposes and for quantum information technology. Regarding the CARS technique applied in the present article, we rely on the previous theoretical and experimental studies by the groups of Tannor, Apkarian, and Pettersson,[14–19] where many aspects of nonlinear optical experiments, dynamics, and interferences in condensed phase have been covered. Zadoyan *et al.*[15,16] have decomposed the I_2 rovibrational coherence using time-gated, frequency-resolved CARS interferograms, the method we are going to use as well. The present scheme is designed to use the control (Kerr gate) pulse duration for variable imaging of the rotational coherence and the quantum beat frequencies, while the excitation pulse timing is crucial in demonstrating a switching functionality for the output of a measurement.

With CN radicals, we are intrigued by the potential to manifest quantum rotational coherence effects in solid state conditions. Applying the preparation, interrogation, and manipulation procedures presented in this paper for a matrix-isolated CN rotor would contribute to the research field of coherent control of rotational degrees of freedom in condensed phase systems. Several studies[20–24] have shown that CN radicals are relatively free rotors when trapped in solid Xe matrices, despite the pronounced, $\sim$1000 cm^{-1} red shift of the electronic $B \leftarrow X$ transition band. The preserved high symmetry of the cavity renders an effectively isotropic interaction potential and decoupling between the impurity and its environment. For CN, under the conditions considered here, bond breaking and vibrational wave packet dynamics are absent processes, as well as their associated losses of phase coherence. The experimental focus can thus be put on rotational decoherence purely, with a minor external perturbation of the system through the driven molecule-host interactions. Here we expect the persistence of quantum coherence due to the rigid and symmetric cage structure of the Xe matrix.

The thermal distribution of rotational states is in general a major source of decoherence.[25] With CN we avoid the creation of massive rovibrational superpositions which happens with femtosecond pulses for the widely studied I_2 molecule. Instead, a single vibrational state space path selects out for CN

a)Electronic mail: toni.k.kiljunen@jyu.fi.

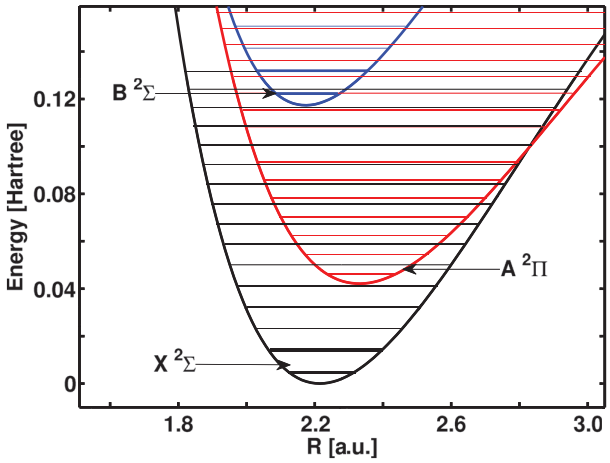

FIG. 1. The three lowest potential energy surfaces $V(R)$ of the CN molecule. The $^2\Sigma$ states are located closely on top of each other yielding a high contrast Franck–Condon selection for a $v' = v''$ transition. Furthermore, the femtosecond laser pulse bandwidths are smaller than the vibrational level separation of ~2000 wavenumbers yielding a state selective excitation scheme for the CARS setup.

with an easily traceable rotational finesse, somewhat similar to rotational coherence spectroscopies. The "pump" pulse can be chosen to create a coherence between the rotational states of the vibronic $v'' = v' = 0$ levels of the X and B states, respectively. The second, "dump" pulse then connects the rotational states from $v' = 0$ with those of the $v'' = 1$ on the ground state X and creates the so-called Raman packet. Finally, the "probe" pulse induces a rotational wave packet belonging to the vibronic level $v' = 1$ on the excited electronic state B. The third-order wave packet then evolves in coherence with the initial state and forms a macroscopic polarization observable in a CARS spectroscopic setup. The vibronic levels drawn together with the potential energy curves in Fig. 1 show the energy gaps of ~2000 cm^{-1}, which is outside the broad wavelength spectrum of the fs-laser pulses. Furthermore, the small inertia renders only a few rotational states occupied at the low temperatures 10 K and 30 K used in this study.

Our aim is to seek for and fiddle with a control knob that utilizes the phase differences of the rotational wave packet to manipulate the spectrum of the anti-Stokes radiation beam. To unravel the control possibilities we proceed in two steps in exemplifying the mechanisms that play a role in the detection of the outcome of the four-wave mixing process. We present time-frequency resolved images involving third- and second-order coherences. Due to the low number of states and rotational connections involved, the interferograms are rather straightforward to interpret. We demonstrate a possibility to manipulate the interferograms by a time-domain parameter that either passively acts in resolving the interference time scales or acts as a mode suppression agent that affects the imaging contrast.

II. THEORY AND METHODS

The third-order polarization $P^{(3)}(t)$ is the material response to three applied fields and therefore serves as a source for the CARS signal. Within time-dependent perturbation theory the contribution to the total polarization vector is

$$P^{(3)}(t) = \sum_{n=0}^{3} \langle \psi^{(n)}(t) | \hat{\mu} | \psi^{(3-n)}(t) \rangle \, . \tag{1}$$

To obtain $P^{(3)}(t)$, the time-dependent Schrödinger equation,

$$i\hbar \frac{\partial |\Psi(t)\rangle}{\partial t} = (\hat{H}_0 - \hat{\mu} E(t)) |\Psi(t)\rangle \tag{2}$$

must be solved for the rovibrational wavefunction $|\Psi(t)\rangle$, which can be expanded in a perturbation series up to third-order as

$$|\Psi(t)\rangle = |\psi^{(0)}(t)\rangle + |\psi^{(1)}(t)\rangle + |\psi^{(2)}(t)\rangle + |\psi^{(3)}(t)\rangle \, , \tag{3}$$

where $|\psi^{(n)}(t)\rangle$ are given iteratively as

$$-i\hbar |\psi^{(n)}(t)\rangle = \int_{-\infty}^{t} \mathrm{d}t' e^{-i\hat{H}_0(t-t')/\hbar} \hat{\mu} E(t') |\psi^{(n-1)}(t')\rangle. \tag{4}$$

Here, $\hat{H}_0$ is the molecular Hamiltonian with known rovibrational eigenstates of the electronic X and B state potential energy curves, while the perturbation is associated with the molecular dipole moment vector $\hat{\mu}$ and the sum field of the consecutive, linearly polarized laser pulses

$$E_p(t) = \epsilon_p(t - \tau_p) e^{-i\omega_p(t-\tau_p) + i\mathbf{k}_p \cdot \mathbf{x}} + \text{c.c.} \, (p = 1, 2, 3), \tag{5}$$

where ω_p is the pulse frequency, $\epsilon_p(t - \tau_p)$ is the pulse envelope function centered at time τ_p, and the indices 1, 2, 3 correspond to pump, dump, and probe pulses, respectively. The spatial dependencies $\mathbf{k}_p$ associated with the pulses become encoded in the wavefunction. As the CARS signal is measured in the anti-Stokes direction $\mathbf{k}_s = \mathbf{k}_1 - \mathbf{k}_2 + \mathbf{k}_3$, under typical conditions (boxcar geometry, time-ordered pulse sequence, low temperature), where ω_2 is nonresonant with the vibronic $v' = 0 \rightarrow v'' = 0$ transition, the expression for $P^{(3)}(t)$ reduces to (Ref. 14)

$$P_s^{(3)}(t) = \langle \psi^{(0)}(t) | \hat{\mu} | \psi^{(3)}_{\mathbf{k}_1 - \mathbf{k}_2 + \mathbf{k}_3}(t) \rangle + \text{c.c.} \, , \tag{6}$$

which can be written in the explicit form

$$\begin{aligned} P_s^{(3)}(T) = \frac{-i}{\hbar^3} \sum_{ifjn} p_i \mu_{if} \int_{-\infty}^{T} \mathrm{d}T_3 \int_{-\infty}^{T_3+\tau_{32}} \mathrm{d}T_2 \int_{-\infty}^{T_2+\tau_{21}} \mathrm{d}T_1 \\ \times e^{-i\omega_{fi}T} [\mu_{fj} \epsilon_3(T_3)] e^{-i(\omega_3 - \omega_{fj})T_3} \\ \times e^{-i\omega_{ji}\tau_{32}} [\mu_{jn} \epsilon_2^*(T_2)] e^{i(\omega_2 - \omega_{nj})T_2} \\ \times e^{-i\omega_{ni}\tau_{21}} [\mu_{ni} \epsilon_1(T_1)] e^{-i(\omega_1 - \omega_{ni})T_1} + \text{c.c.} \end{aligned} \tag{7}$$

The time variables here are defined as $T = t - \tau_3$, $T_p = t_p - \tau_p$, and the time delays are $\tau_{32} = \tau_3 - \tau_2$ and $\tau_{21} = \tau_2 - \tau_1$. The indices refer to the energy level connections $i \rightarrow n \rightarrow j \rightarrow f$ through which the polarization builds up in the molecule, see Fig. 2. The path involves fixed vibrational quantum numbers $0 \rightarrow 0 \rightarrow 1 \rightarrow 1$, respectively, and due to the selection rules, the rotational route complexity is sixfold at most. For initial rotational levels N_i equal to 0 and 1, there can be only two and five routes, respectively.

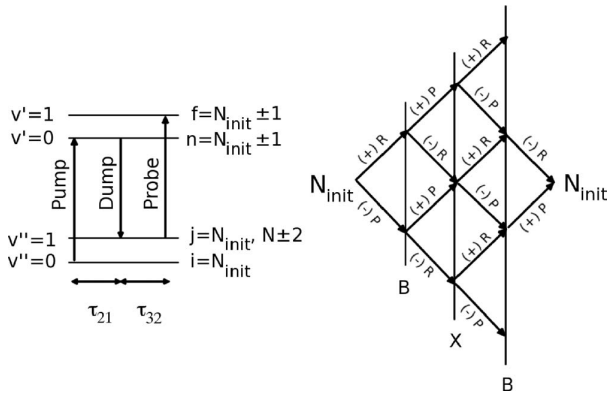

FIG. 2. Schematic representation of the creation of the third-order polarization by the three time-delayed laser pulses pump, dump, and probe. Left panel shows the (ro-)vibronic transition path $i \rightarrow n \rightarrow j \rightarrow f$ alternating between the $X^2\Sigma$ and $B^2\Sigma$ electronic states. Right panel shows the rotational connection diagram for the six possible routes from the initial level N_i ($v'' = 0$). P and R represent the two allowed rotational branches while plus and minus signs denote a change in the rotational quantum number N for each of the four transitions.

A. Interferences

The electric dipole moment matrix elements in Eq. (7) connect rotational states within a single vibrational state, i.e., the nth pulse creates a wave packet that has 2^n rotational components, each transition scaled by a proper Hönl–London type factor.[26] The total polarization can be seen to oscillate at frequency differences between the initial level and a level occupied at various instants. After the probe pulse, for instance, the difference $\omega_{fi} = \omega_f - \omega_i$ corresponds to the anti-Stokes radiation at the P and R branches. The index f thus includes $N_i - 1$ and $N_i + 1$ rotational state coherences, respectively, on the $v' = 1$ level of the B state. The two sources of radiation show a beating during the time T when the radiation is detected, as will be discussed in Sec. III A. The beat wavenumber is (for $N_i > 1$)

$$\tilde{\nu}_{\mathrm{RP}}^{(ii)} = 2B_{1,B}(2N_i + 1)\,, \tag{8}$$

where $B_{1,B}$ is the level-specific rotational constant on the excited electronic state. Thermal distribution of initial rotational states appears in Eq. (7) through the summation weighted by the Boltzmann factors p_i. This leads to a distribution of P,R pairs detectable in a signal, which can be written in a form (Ref. 14)

$$S \propto \sum_{ii',ff'} e^{-i(\omega_{fi} - \omega_{f'i'})T} + \mathrm{c.c.} \tag{9}$$

As a result, the following three types of intra- and inter-branch interference terms (difference wavenumbers) arise from the radiation beam

$$\tilde{\nu}_{\mathrm{RR}}^{(i,i-\eta)} = 2\eta N_i(B_{1,B} - B_{0,X}) + \eta[B_{1,B}(3-\eta) + B_{0,X}(\eta - 1)]\,, \tag{10}$$

$$\tilde{\nu}_{\mathrm{PP}}^{(i-\eta,i)} = -2\eta N_i(B_{1,B} - B_{0,X}) + \eta[B_{1,B}(1+\eta) + B_{0,X}(1-\eta)]\,, \tag{11}$$

$$\tilde{\nu}_{\mathrm{RP}}^{(i,i\pm\eta)} = 2B_{1,B}(2N_i + 1) \pm \eta(B_{1,B} + B_{0,X}) - (\eta^2 \pm 2\eta N_i)(B_{1,B} - B_{0,X})\,, \tag{12}$$

where the interference order parameter η is the difference between the initial quantum numbers N_i. The interference results in a signal oscillation pattern and includes both intra- and intermolecular contributions. The total number of modulations is $(m^2 - m)/2$, where m is the number of transitions $f \rightarrow i$. The intramolecular beat spans the interval 2.872–0.663 ps for the states N_i = 1–6, respectively. For the adjacent levels ($\eta = 1$), one obtains 8.419–7.551 ps and 9.042–10.031 ps intervals for the R and P branches, respectively, while the interbranch contributions $\tilde{\nu}_{\mathrm{RP}}^{\pm}$ are faster, between 4.360 and 0.710 ps.

On the other hand, during the time interval τ_{32} between the dump and probe pulses, the polarization phase develops according to the frequency difference ω_{ji} on the X state, as will be discussed in Sec. III B. Considering the two branches of radiation, the time delay introduces the wave packet intramolecular interference terms

$$\tilde{\nu}_{\mathrm{R}}^{(i)} = B_{1,X}(4N_i + 6), \tag{13}$$

$$\tilde{\nu}_{\mathrm{P}}^{(i)} = B_{1,X}(4N_i - 2)\,, \quad N_i > 1 \tag{14}$$

between the rotational routes (++ −) and (+− +), (−+ +) for the R, and between (−− +) and (−+ −), (+− −) for the P, see Fig. 2. We use these wavenumbers as a wave packet interferometry tool. For the states occupied below 30 K (N_i = 0–6), the numbers cover the range of ∼11–56 cm^{-1} (2.968–0.594 ps). The other form of intramolecular interference occurs between the branches, where the $j = i + 2$ and $j = i - 2$ members of the wave packet produce interference terms at $4B_{1,X}(2N_i + 1)$ wavenumbers ($N_i > 1$). Detection of the above and intermolecular interferences is sensitive to the lifetime of the induced polarization dictating the resolution power.[14] Polarization contributions originating from the adjacent initial levels dominate the intermolecular effect, as they emerge spectrally apart by only $2B_{1,X}$.

B. Detection methods

A detection of the CARS beam would already serve as a manifestation of the electronic coherence. Imaging the interference as signal oscillations or resolving it into the P and R branches would further authenticate the sought-after rovibronic coherence in the solid state. Here we examine the frequency resolution of the rotational coherences by two time delays. First, we employ for the signal detection a time-delayed gate pulse which samples the beam during the time T, i.e., after the preparation of the third-order polarization. This provides us with a convenient imaging method for the coherence. Then, we illustrate how controlling can be exerted on the image by the probe delay variable τ_{32}, which affects the emergence of the two branches via the periodicity through Eqs. (13) and (14).

In the first case, both pulse time delays τ_{32} and τ_{21} remain fixed and the outcome is a time-frequency resolved

image of a single measurement. In the time-gated CARS experiments, the signal consists of time slices of the anti-Stokes beam which are each dispersed through a monochromator. This can be suitably presented by taking a Husimi transform of the radiation. Due to the square-law detection, the two-dimensional, time-gated CARS images are then of form

$$S(\omega_0, t_g) = \left| \int_{-\infty}^{\infty} \mathrm{d}T\, e^{-\alpha(T-t_g)^2 - i\omega_0(T-t_g)} i P_s^{(3)}(T) \right|^2, \quad (15)$$

where t_g is the scanned gate delay while the gate width δt ($\alpha = 2\ln 2/\delta t^2$) sets the resolution in the time-frequency plane. The width of the gate is adjusted comparable to the periods of oscillation due to the beating given by Eqs. (10)–(12). The logic is that for gate widths shorter than the beating period, the wavenumber resolution power is suppressed and the interference effects survive as a time oscillation of the signal, providing a complementary view to the composition of the wave packets and the polarization. The second scenario to observe the third-order polarization is to align the anti-Stokes beam without gating to a monochromator, and then to record the homodyned signal in the time-integrated mode. This number is seen in Eq. (7) to depend on the time delays such that the signal becomes oscillatory corresponding to ω_{ji} and ω_{ni}. We consider the second-order coherence evolution by scanning the the dump–probe delay and fixing the τ_{21}. The two-dimensional, time-integrated CARS image is thus computed as

$$S(\omega_0, \tau_{32}) = \left| \int_{-\infty}^{\infty} \mathrm{d}T\, e^{-i\omega_0 T} i P_s^{(3)}(T; \tau_{32}) \right|^2. \quad (16)$$

If the polarization is presumed long-lived, the spectrum is well resolved and the intermolecular interferences in the signal are suppressed.

C. Implementation methods

The implementation for computing the polarization numerically follows the work on vibrational wave packets.[14,19,27,28] In particular, the iterative form for the rotational route component r of the nth order wave packet is

$$|\psi_r^{(n)}(t+\Delta t)\rangle = e^{-i\hat{H}_0\Delta t/\hbar}|\psi_r^{(n)}(t)\rangle + \frac{i}{\hbar}\Delta t \mu_{rr'} E_n(t+\Delta t)|\psi_{r'}^{(n-1)}(t+\Delta t)\rangle. \quad (17)$$

The 0-0-1-1 path in the vibrational state space was chosen to maximize the Franck–Condon factors. With the present Morse potential functions $V(R)$ shown in Fig. 1, the corresponding pump, dump, and probe laser pulse carrier wavelengths are 388, 423, and 388 nm, respectively, while the anti-Stokes beam obtains at 358 nm. The rotational energies are incorporated in the wave packet propagation through the potential curves as

$$V_r(R) = V(R) + \hbar^2 N(N+1)/2MR^2, \quad (18)$$

where M is the reduced mass of the molecule. The rotational constants obtained as expectation values with the above potential are found, in excellent agreement with the experimental values,[29] to be the following (in cm^{-1}): $B_{1,B} = 1.9356$, $B_{0,B} = 1.9594$, $B_{1,X} = 1.8731$, and $B_{0,X} = 1.8901$. In order to remain at the weak field regime, we have set the pulse amplitude envelope maxima to 10^{-4} a.u. The dipole moment for the parallel transition between the electronic states X and B was considered to be a constant value at 0.7 a.u.[30] A bookkeeping routine was applied to account for the rotational strength factors $\sum_{M_N''} \langle N', M_N'| \cos\theta |N'', M_N''\rangle$ for each of the routes. The pulse widths (intensity FWHM) were set to transform-limited 50 fs. We set the τ_{21} to a nonoverlapping 200 fs to saturate the Raman packet amplitude on the ground state molecule. The rotational superposition appears purely as a phase evolution, where the relative timing among the packet depends on delay times. A decay of coherence can be introduced by multiplying the polarization $P_s^{(3)}(T)$ by an exponential $e^{-\gamma T}$. Schallmoser *et al.*[21] have estimated a rotational relaxation rate of about 100 GHz for CN in solid Xe, which we shall use in Sec. III B. The number results from line widths of the infrared emission spectrum that belongs to the $X^2\Sigma$ state $\Delta v = 1$–3 transitions. Observations[21] of the weak Q branch due to a rotational barrier, and the related shift of the rotational constant ($B_e \approx 1.6$ cm^{-1}) due to an induced Xe matrix inertia, are bypassed at the present account.

III. RESULTS AND DISCUSSION

Fourier transform of the anti-Stokes beam can be used to reveal the splitting into initial-state specific contributions ω_{fi} in the two branches. Relative to the vibronic transition origin at $\tilde{\nu} = 27922$ cm^{-1} (358 nm), the radiation field contains the displaced wavenumbers

$$\tilde{\nu}_{\mathrm{R}}^{(i)} = 2B_{1,B} + N_i(3B_{1,B} - B_{0,X}) + N_i^2(B_{1,B} - B_{0,X}), \quad (19)$$

$$\tilde{\nu}_{\mathrm{P}}^{(i)} \overset{N_i \geq 1}{=} -N_i(B_{1,B} + B_{0,X}) + N_i^2(B_{1,B} - B_{0,X}), \quad (20)$$

similarly to conventional vibration-rotation spectra. Noting the small difference of rotational constants, one obtains $\sim 2B$ line spacing. Interference of the branches, on the other hand, can be revealed by the time-gated detection. Besides the temperature and population evolution effects, the six components of a rotational wave packet give a varying "R to P ratio" composition for the $P_s^{(3)}$ as a function of the initial state. This is a result of the transition probabilities which are rather sensitive to the present low values of N. While the $N_i = 0$ case is of R type purely, we obtain the following R-branch excess percentages for $N_i = 1 - 6$, respectively: 97, 46, 28, 18, 12, and 8 (i.e., the last R:P-ratio is 1.08:1). These ratios are computed by comparing the coherence amplitudes $\langle \psi^{(0)}|\mu_r|\psi_r^{(3)}\rangle + c.c.$, where μ_r represents a rotational strength factor for a combination of four transitions $i \to n \to j \to f \to i$. One finds a moderate bias for the anti-Stokes radiation to be channeled into the R-branch according to μ_r, where $r = (++-)$ route contributing to R-branch is the dominant component, see Fig. 2.

A. Interferometric imaging

For an ensemble of rotational initial states the polarization interference emerges in several combinations of the

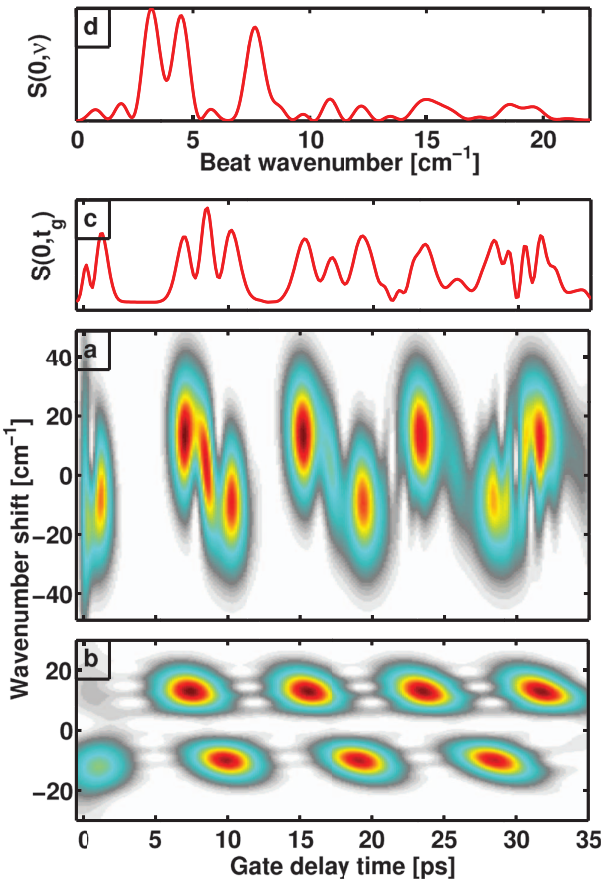

FIG. 3. The time-gated images as obtained by the use of Eq. (15) for two gate widths (a) 500 fs and (b) 3 ps, where thermal distributions correspond to the 30 K case. The wavenumber scale relative to the anti-Stokes origin at 27922 cm^{-1} separates the R branch emission (positive side) from the P branch (negative). The upper interferogram shows a signal oscillation pattern between the R and P branches (at the zero wavenumber shift) and carries information about the rotational wave packet in the time domain. Panel (b) case approaches the spectrally resolved limit leaving only the next-neighbor polarization beating visible. Panel (c) shows the shift-zero cut $S(0, t_g)$ of the panel (a) signal, and panel (d) shows the FFT power spectrum $S(0, \tilde{\nu})$ of the panel (c) trace resolving the interference as separable quantum and intermolecular beats.

transition wavenumbers. They can be grouped into combinations within a branch and between branches. The time-gated CARS signals obtained with pulses fixed at $\tau_{21} = \tau_{32} = 200$ fs intervals are shown in Fig. 3 for the 30 K case. Detection of such a signal is simulated by the Husimi transform plot [Eq. (15)], where the Kerr gate delay extends to 35 ps and its width is either (a) 500 fs or (b) 3 ps. The two representative widths are chosen to capture different features of the signal modulation. The figure exhibits the possibility to experimentally control the rotational coherence imaging by CARS. In case (a), the plot shows rapid beatings as the wavenumber resolution is compromised by the short time slice. The question is, which of the many beats shall dominate the image. In addition to the RR and PP contributions occurring at 8.7 ps on average, also the faster combinations have a period multiple overlapping at this region which leads to the intensity maxima. The interbranch beatings (RP) are washed out in case (b), where the R and P branches are separated but not resolved. A hint from the rotational line structure can be seen between the bright spots; however, for a stick spectrum one would need a gate width $\delta t > 10$ ps. The remaining oscillation in panel (b) is due to the RR and PP intermolecular beats [Eqs. (10) and (11)].

Fourier transforms of the gated-signal cuts as in Fig. 3 panels c-d render the fast beating back to the wavenumber domain. A signal trace transformed at zero wavenumber shift reveals a dominant peak region at a low wavenumber (∼4 cm^{-1}, $\eta = 1$) regime. This is followed by an $\eta = 2$ intermediate intensity region at 7–8 cm^{-1} while higher wavenumbers are low in intensity (FFT power). A closer inspection of the image shows the ∼8.1 and 9.3 ps modulations in branches R and P, respectively, to correspond best with the N_i levels 2–3. These are also the levels that give the most intense peaks in a direct Fourier transform of the anti-Stokes radiation beam.

The concept can be illustrated to utmost detail by considering a specific sample, where just $N_i = 1, 2$ initial levels are set to be occupied. Then the polarization interference emerges in six combinations only: (intramolecular) $\tilde{\nu}_{\mathrm{RP}}^{(22)}$ and $\tilde{\nu}_{\mathrm{RP}}^{(11)}$ with 1.723 and 2.872 ps periods, (intermolecular, interbranch) $\tilde{\nu}_{\mathrm{RP}}^{(1,2)}$ and $\tilde{\nu}_{\mathrm{RP}}^{(2,1)}$ with 2.180 and 2.129 ps periods, and (intrabranch) $\tilde{\nu}_{\mathrm{RR}}^{(2,1)}$ and $\tilde{\nu}_{\mathrm{PP}}^{(1,2)}$ with 8.230 and 9.042 ps periods, respectively. The 3 ps gate width again leaves only the latter two contributions spectrally unresolved, whilst the 500 fs gate is too short to uncouple the interbranch modulation and a spectrogram contains all the information in the time domain. Despite the absence of the higher order interferences, this leads to a *more* complicated beating pattern than in the full Boltzmann case above, since, now there is a narrower state distribution so that phase cancellations become ineffective. The transform procedure resolves the interferences such that the fastest quantum beat $\tilde{\nu}_{\mathrm{RP}}^{(22)}$ at 19.4 cm^{-1} remains strong in intensity. The number of components rather than the 500 fs gate window appears as the key determining factor in suppressing fast oscillations and producing the silent intervals in the spectrogram image of Fig. 3(a). The adjacent levels ($\eta = 1$) give the prevailing feature at $\sim(2Bc)^{-1}$, which is also the period where overlapping multiples of higher order contributions occur, resulting in net signal amplification. Thus the observed periodicity here and before[15,16] is of full revival type whilst the fractional revivals are weaker. The situation is similar to coherent alignment dynamics,[31] where the revival period is governed by the least common multiple of the frequencies associated with the rotational wave packet.

B. Time-integrated spectrograms

The anti-Stokes radiation beam coupled into a spectrometer is presented as a function of the time delay τ_{32} in Fig. 4. The time-integrated, square-law detected signal is computed by Eq. (16) for 10 K conditions. The resolution in wavenumber domain is dictated by the decay parameter $\gamma = 0.1$ ps^{-1} applied for the third-order polarization, which is integrated up to 40 ps. The delay time is extended up to 15 ps in Fig. 4, and no decay parameter was introduced for this part of the evolution. We note that for iodine at 10 K, the dephasing rate for

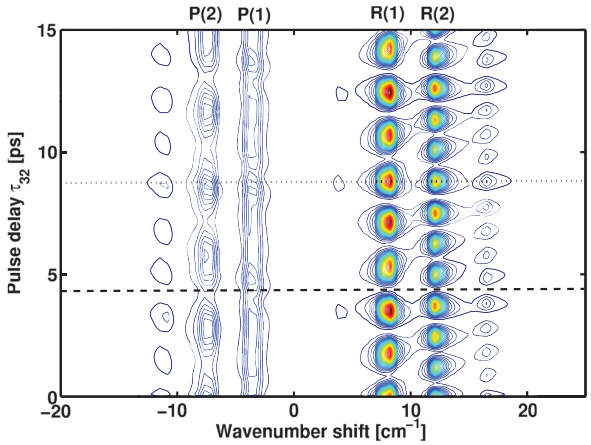

FIG. 4. The time-integrated frequency-resolved CARS interferogram for the 10 K ensemble of wave packets as obtained by the use of Eq. (16). The contour level increment corresponds to 4% of the intensity maximum. Labeling corresponds to the most intense P and R branch traces. The dashed and dotted lines denote intervals for a global intensity minimum and a maximum, respectively, which relates to a dimmer switch function of the pulse delay.

low vibrational levels on the ground state was found[19] to be well below 0.01 ps^{-1}. The image of the second-order coherence reveals the beatings in resolved R(N_i) and P(N_i) line contributions according to Eqs. (13) and (14), respectively. The most intense line in the interferogram is the R(1) at +7.8 cm^{-1} [Eq. (19)] with the 1.78 ps oscillation period. Oscillations in R(2) and R(3) lines are 1.4 and 1.8 times faster, respectively. R(0) is weak due to low Boltzmann weight (0.142) and its 2.97 ps (0.6 times slower) period is not visible. However, a trace of the R(0) radiation surfaces due to the amplification from the neighboring strong R(1) line. The same type of amplification is also present on top of the P(1) line at −3.8 cm^{-1} which should not show a τ_{32} dependent intensity modulation at all since only the $j = 1$ route is available for a wave packet. Shortening the decay time broadens the spectral lines and leads to intermolecular interference, i.e., the phenomenon called polarization beating in the earlier time-resolved CARS studies.[14,19]

It becomes obvious now by inspecting Fig. 4 that varying the delay time affects the spectrum. For example, at 4.45 ps (which happens to be 2.5, 3.5, and 4.5 times the R(1), R(2), and R(3) periods, respectively) there is clearly a "node" in the modulation pattern (dashed line). Put analytically, the intensity minima occurring at every

$$t_N = \frac{1}{2cB_{1,X}} \frac{2l+1}{4N+b}, \quad l = 0, 1, \ldots, \tag{21}$$

coincide, when $l = N + 1$ in the R branch and when $l = N - 1$ in the P. This is due to the $4B_{1,X}$ step in Eqs. (13) and (14). In Eq. (21), N is the branch index and b is 6 or −2 for R or P, respectively. The first constructive phase accumulation (dotted line in Fig. 4) then takes place at the double time (8.90 ps), i.e., at $2N + 3$ or $2N - 1$ times the oscillation period in R or P branches, respectively. These extrema represent the on/off switch of the total emission intensity.

C. Controlling the interferograms

Here we present a synthesis of the above two analyses of the coherences. Knowing the wave packet interference terms allows us to engineer the emerging spectrum as well as the time-gated interferograms. While the above discussed scrutiny with τ_{32} affects more globally the signal intensities in an on/off fashion, one can also select the delay time aimed at quenching a certain ω_{fi} line contribution. We revisit the time-gated imaging here by considering a couple of different values for the dump–probe time delay. For instance, by setting $\tau_{32} = 890$ fs, 636 fs, and 495 fs we sample the nodes of R(1)&P(2), R(2)&P(3), and R(3)&P(4), respectively. A standard monochromator view of the spectrum comb can be used to reveal the dependence of the ω_{fi} component amplitudes on the delay. One observes, for example, that at 10 K the R branch bias can be turned into P branch bias by increasing the delay from 200 fs to 636 fs. At 30 K, quenching the whole P branch is effective at $\tau_{32} = 890$ and 636 fs.

Three types of manipulation have been discussed above. (1) The overall brightness of the signal can be accessed by the use of common nodal structure [Eq. (21)] in the oscillation pattern. (2) Suppression or enhancement of individual spectral components and their associated interferences in a signal obtains by tuning into half revivals [Eqs. (13) and (14)]. (3) Selection between R and P branch dominance can be rated by 1D representations of the CARS beam components. The Husimi representations in Fig. 5 illustrate the latter effect, where switching of light from the R branch to P branch is achieved by changing the delay time τ_{32} from the 890 fs (left panels) to the 495 fs (right side) at the 30 K conditions. The time-gate has to be shorter than the oscillation period to capture the beating features. A 500 fs FWHM Kerr gate (e.g., CS_2)[32] is well-suited for the fastest events. The 3 ps width is chosen to better highlight the switching functionality.

Regarding the experimental realization of the present ideas for illustrating rotational coherence in solid state conditions, the following practicalities need to be considered. First is the wavelength adjustment, as the transitions occur

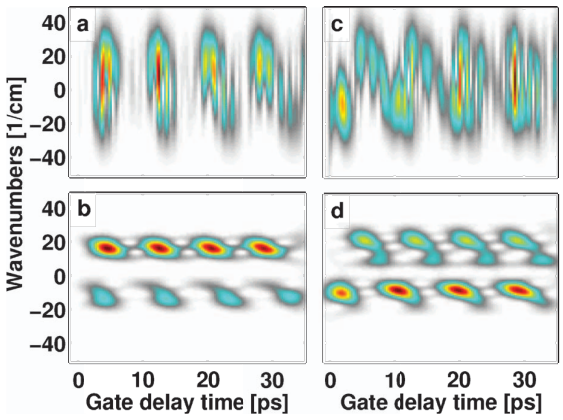

FIG. 5. 2D spectrograms for the CARS signal for two values of the control parameter τ_{32}: 890 fs (a,b) and 495 fs (c,d). Images show the light switching functionality between the branches. The interferogram bandwidths are set by the gate durations 500 fs (a,c) and 3 ps (b,d) which demonstrates the temporal versus spectral resolving power.

shifted from the present gas phase values. Second, the balance between the low mobility of HCN dissociation fragments at low temperatures and the good matrix quality at elevated temperatures is going to be critical for a successful experiment. Obviously, one is not limited to the present mode of detection for a rotational coherence. In particular, degenerate FWM with $v = 0$ path throughout applies nicely to the CN system with the price that additional terms in Eq. (1) survive to diversify the signal.[27] The SiN radical is isovalent to CN and exhibits a similar level structure, but we are unaware of its rotational properties in matrix isolation. One can ponder controlling the rotation itself by the (non)resonant alignment or Raman induced polarization spectroscopy methods, where time evolution is detected nonintrusively by the optical Kerr effect.[33,34] For the nonresonant techniques, one is more flexible regarding the molecular level structure as the rotational wave packet is generated on the ground state. N_2, for example, is a thoroughly investigated molecule with respect to alignment dynamics.[35] The only question is, to which degree is the rotation hindered in a rare gas solid? Finally, it should be mentioned that other solid hosts than the rare gases can be taken into account. In particular, the parahydrogen as a soft quantum crystal can be considered as a minimally perturbing medium.

IV. CONCLUSIONS

We use four-wave mixing to manipulate rotational coherence of CN molecules, and discuss extending this scheme into the condensed phase. Because of the suitable level structure of the molecule, we attain with femtosecond pulses a state selection that resembles a narrow band excitation. In particular, we choose a single vibrational state with each pulse excitation, and the rotational structure is bound by selection rules to depend on the initial state. At the low temperatures of this study, the number of rotational levels is limited to a few. These conditions allow for a detailed investigation of the FWM signal. The signal is represented as an interferogram image which is controllable by the Kerr gate width and the excitation pulse delay parameters. The results show much simpler interferograms than obtained earlier by Zadoyan *et al.*[15,16] for the rovibrational wave packets of iodine.

The FWM method with CN molecule exhibits two intrinsic time scales. The third-order coherence has a periodicity range of 0.7–10.0 ps, which sets the demands for the time gating in the interferometric imaging. Interference can be visualized fully, if the gate pulse duration is shorter than the revolution of the rotational ensemble. The use of longer gate widths are demonstrated to filter out the intramolecular interference and enable focussing on the polarization beating, that dominantly emerges from adjacent rotational energy levels due to the full revival type phase accumulation. This necessitates, on the other hand, a sufficiently persistent coherence on the excited electronic state whence the radiation originates. The coherence decay comes into play by another mechanism, i.e., it can shorten the detection integration time and allow for intermolecular interference to emerge as in conventional time-resolved CARS experiments.[14] In the present case, however, the empirically set decay is ineffective enough such that the time-integrated mode of detection is spectrally resolved. The dump–probe delay of the laser pulses can then be used to fine tune the signal by suppressing or enhancing chosen P or R branch rotational contributions, without changing the composition of the rotational wave packet itself. This represents a contrary case to the approach, where the molecular rotational *population* is controlled by wave packet interference using two strong laser pulses.[36–38] Here, interference is used for the detection purpose, to control the texture of the emerging image.

In a sense the present work is a fusion of two original coherent control aspects: excitation-path interference and pulse-sequence timing.[28] The computations utilize the time difference of the dump and probe pulses as the single control parameter, thus resembling the Tannor–Rice–Kosloff scheme. At the same time, the Brumer–Shapiro scheme of coherent control, which is based on interferences between excitation paths leading to the same final state, is touched upon as the Raman packet involves definite rotational routes. Here in CARS, the final state is met at closing of the time-circuit diagram upon projecting the third-order wave packet on the time-evolved ground state. We do not operate with the relative phase of the excitation pulses, but let the phases of the intermediate states affect the final outcome, which is the spectrogram image. The interferogram figures presented exhibit the possibility to experimentally control the rotational coherence imaging by the CARS method.

ACKNOWLEDGMENTS

T. K. and J. L. were supported by the Academy of Finland decision no. 124974.

[1] G. A. Worth and C. Sanz Sanz, Phys. Chem. Chem. Phys. **12**, 15570 (2010).
[2] T. Brixner and G. Gerber, ChemPhysChem **4**, 418 (2003).
[3] M. Dantus and V. V. Lozovoy, Chem. Rev. **104**, 1813 (2004).
[4] P. Nuernberger, G. Vogt, T. Brixner, and G. Gerber, Phys. Chem. Chem. Phys. **9**, 2470 (2007).
[5] S. O. Konorov, X. G. Xu, J. W. Hepburn, and V. Milner, J. Chem. Phys. **130**, 234505 (2009).
[6] P. M. Felker, J. Phys. Chem. **96**, 7844 (1992).
[7] M. F. Gelin, C. Riehn, M. Kunitski, and B. Brutschy, J. Chem. Phys. **132**, 134301 (2010).
[8] J. A. Cina, Annu. Rev. Phys. Chem. **59**, 319 (2008).
[9] K. Ohmori, Annu. Rev. Phys. Chem. **60**, 487 (2009).
[10] H. Katsuki, H. Chiba, C. Meier, B. Girard, and K. Ohmori, Phys. Chem. Chem. Phys. **12**, 5189 (2010).
[11] E.-B. W. Lerch, X. Dai, S. Gilb, E. A. Torres, and S. R. Leone, J. Chem. Phys. **124**, 044306 (2006).
[12] N. F. Scherer, A. Matro, L. D. Ziegler, M. Du, R. J. Carlson, J. A. Cina, and G. R. Fleming, J. Chem. Phys. **96**, 4180 (1992).
[13] H. Goto, H. Katsuki, H. Ibrahim, H. Chiba, and K. Ohmori, Nat. Phys. **7**, 383 (2011).
[14] J. Faeder, I. Pinkas, G. Knopp, Y. Prior, and D. J. Tannor, J. Chem. Phys. **115**, 8440 (2001).
[15] R. Zadoyan and V. A. Apkarian, Chem. Phys. Lett. **326**, 1 (2000).
[16] R. Zadoyan, D. Kohen, D. A. Lidar, and V. A. Apkarian, Chem. Phys. **266**, 323 (2001).
[17] M. Karavitis, R. Zadoyan, and V. A. Apkarian, J. Chem. Phys. **114**, 4131 (2001).
[18] M. Karavitis, T. Kumada, I. U. Goldschleger, and V. A. Apkarian, Phys. Chem. Chem. Phys. **7**, 791 (2005).
[19] T. Kiviniemi, T. Kiljunen, and M. Pettersson, J. Chem. Phys. **125**, 164502 (2006).
[20] W. C. Easley and W. Weltner, Jr., J. Chem. Phys. **52**, 197 (1970).
[21] G. Schallmoser, A. Thoma, B. E. Wurfel, and V. E. Bondybey, Chem. Phys. Lett. **219**, 101 (1994).

[22]A. Thoma, G. Schallmoser, A. M. Smith, B. E. Wurfel, and V. E. Bondybey, J. Chem. Phys. **100**, 5387 (1994).
[23]M. Pettersson, J. Lundell, L. Khriachtchev, and M. Räsänen, J. Chem. Phys. **109**, 618 (1998).
[24]S. L. Fiedler, K. Vaskonen, J. Ahokas, H. Kunttu, J. Eloranta, and V. A. Apkarian, J. Chem. Phys. **117**, 8867 (2002).
[25]K. Ohmori, Y. Sato, E. E. Nikitin, and S. A. Rice, Phys. Rev. Lett. **91**, 243003 (2003).
[26]R. N. Zare, *Angular Momentum* (Wiley, New York, 1988).
[27]S. Meyer and V. Engel, J. Raman spectrosc. **31**, 33 (2000).
[28]D. J. Tannor, *Introduction to Quantum Mechanics: A Time-Dependent Perspective* (University Science Books, Sausalito, 2007).
[29]K. P. Huber and G. Herzberg, *Constants of Diatomic Molecules* (Van Nostrand Reinhold, New York, 1979).
[30]P. J. Knowles, H.-J. Werner, P. Jeffrey, and D. C. Cartwright, J. Chem. Phys **89**, 7334 (1988).
[31]P. W. Dooley, I. V. Litvinyuk, K. F. Lee, D. M. Rayner, M. Spanner, D. M. Villeneuve, and P. B. Corkum, Phys. Rev. A **68**, 023406 (2003).
[32]T. Steffen, N. A. C. M. Meinders, and K. Duppen, J. Phys. Chem. A **102**, 4213 (1998).
[33]V. Renard, M. Renard, A. Rouzée, S. Guérin, H. R. Jauslin, B. Lavorel, and O. Faucher, Phys. Rev. A **70**, 033420 (2004).
[34]M. Renard, E. Hertz, B. Lavorel, and O. Faucher, Phys. Rev. A **69**, 043401 (2004).
[35]N. Owschimikow, F. Königsmann, J. Maurer, P. Giese, A. Ott, B. Schmidt, and N. Schwentner, J. Chem. Phys. **133**, 044311 (2010).
[36]A. S. Meijer, Y. Zhang, D. H. Parker, W. J. van der Zande, A. Gijsbertsen, and M. J. J. Vrakking, Phys. Rev. A **76**, 023411 (2007).
[37]C. Wu, G. Zeng, Y. Gao, N. Xu, L.-Y. Peng, H. Jiang, and Q. Gong, J. Chem. Phys. **130**, 231102 (2009).
[38]N. Owschimikow, B. Schmidt, and N. Schwentner, Phys. Rev. A **80**, 053409 (2009).